Supporting Information

Interface engineering of *fcc*-RuCo@*hcp*-Ru core-shell nanoplates for efficient industrial alkaline hydrogen evolution

Shihuan Hong[a], Ning Song[a], Wenli Zhang[a], Deping Wang[a], Lichun Liu[b], Hongjun Dong[a], Yang-Yang Yu[c]*, Chunmei Li[a]**

[a]Institute of Green Chemistry and Chemical Technology, School of Chemistry and Chemical Engineering, Jiangsu University, Zhenjiang 212013, P.R. China.

[b]College of Biological, Chemical Sciences and Engineering & Nanotechnology Research Institute, Jiaxing University, Jiaxing 314001, P.R. China

[c]Information Materials and Intelligent Sensing Laboratory of Anhui Province, Institutes of Physical Science and Information Technology, Anhui University, Hefei 230601, P.R. China.

*Corresponding authors: E-mail: lichun.liu@zjxu.edu.cn; yyyu@ahu.edu.cn; lichun_mei_happy@126.com

Experimental section

Chemicals. Platinum on carbon (Pt/C,5 wt %, AR), ruthenium(III) chloride ($RuCl_3$, 99%, AR) were purchased from Shanghai Macklin Biochemical Co., Ltd. Cobalt(II) chloride ($CoCl_2$, 98%, AR), potassium hydroxide (KOH, 99%, AR), polyvinylpyrrolidone (PVP, MW=8000) were purchased from Aladdin Chemical Reagents Co., Ltd. Formaldehyde (HCHO), acetone (≥ 99.5%, AR), ethanol (AR) were purchased from Sinopharm Chemical Reagent Co., Ltd. Nafion (5 wt %, AR) was purchased from Alfa Aesar. Deionized (DI) water was employed as solvent.

Synthesis of the samples. A mixture of 0.12 mmol ruthenium(III) chloride ($RuCl_3$) and 0.4 mmol cobalt(II) chloride ($CoCl_2$) was dissolved in 20 mL deionized water and stirred at room temperature for 15 minutes to form a homogeneous solution. Subsequently, 100 mg polyvinylpyrrolidone (PVP) and 2 mL formaldehyde (HCHO) were added, and stirring was continued for 4 hours to reduce the metal precursors and initiate nanoparticle nucleation. The dispersed solution was transferred into a 50 mL Teflon-lined stainless-steel autoclave and subjected to hydrothermal treatment at 160 ℃ for 4 hours, inducing a crystal phase transition (coexisting face-centered cubic, *fcc*, and hexagonal close-packed, *hcp*, phases). After natural cooling to room temperature, the product was collected by centrifugation at 16,000 rpm for 5 minutes and washed three times with acetone and ethanol, respectively, to remove impurities. The final product, $Ru_{12}(fcc_{0.86})Co_{40}@Ru_{12}(hcp_{0.14})$ nanoparticles with a heterostructure, was obtained. By adjusting the initial Ru:Co molar ratios (6:46, 26:26, 40:12, 52:0), other samples—including $Ru_6(fcc_{0.84})Co_{46}@Ru_6(hcp_{0.16})$, $Ru_{26}(fcc_{0.88})Co_{26}@Ru_{26}(hcp_{0.12})$, $Ru_{40}(fcc_{0.90})Co_{12}@Ru_{40}(hcp_{0.10})$, and pure *hcp*-phase Ru_{hcp} were synthesized.

Preparation the working electrode. Typically, the ink was prepared by dispersing 5 mg of samples into a 1 mL mixture containing 960 μL of ethanol and 40 μL of Nafion (5 wt %) with ultrasonic treatment for 30 minutes. Subsequently, the prepared ink of all catalysts was deposited onto carbon paper (0.25 × 0.25 cm^2) to achieve a loading density of 2.4 mg cm^{-2}. After drying, the working electrodes were obtained. Electrochemical tests were conducted using a VERSTAT-3 (Princeton Applied Research, America) electrochemical workstation with a conventional three-electrode

system at room temperature. In this system, the sample-coated carbon paper electrode served as the working electrode, while the Hg/HgO electrode and platinum sheet acted as the reference and counter electrodes, respectively. 1 M KOH solution was utilized as the electrolyte.

Materials characterization. X-ray diffraction (XRD) was recorded by a D/MAX-2500 diffractometer (Rigaku, Japan) with a Cu Kα radiation source from 10−80º. Transmission electron microscopy (TEM), high-magnification TEM (HRTEM), and scanning TEM (STEM) images were conducted on H-7800 electron microscope with an accelerating voltage of 200 kV. In addition, the chemical state of the sample was studied by the X-ray photoelectron spectroscopy (XPS) (Thermo Scientific K-Alpha). All XPS spectra were corrected using the C 1s line at 284.6 eV. Curve fitting and background subtraction were accomplished. The content of catalyst was characterized by Inductively Coupled Plasma Optical Emission Spectrometry (ICP-OES 5800). The Brunauer-Emmett-Teller (BET) specific surface area and average pore diameter distribution were recorded by using a Micromeritics TriStar II3020 instrument.

In-situ Raman study: In-situ Raman study was carried out with a confocal microscopic Raman spectrometer (LabRam HR, Horiba, France). To enhance the signal intensity, a strategy called shell-isolated nanoparticle enhanced Raman spectroscopy (SHINERS) **was employed**. Briefly, 55 nm Au nanoparticles coated with a layer of 2 nm SiO_2 (SHINs) was prepared according to their protocol, and the surface-enhanced Raman spectroscopy (SERS) effect as well as the completeness of the SiO_2 shell were confirmed with pyridine as a probing molecule. To load the catalyst and SHINs, catalyst was dispersed in the water to a concentration of 1 mg mL^{-1}. 20 μL of dispersion was dropped on a polished Au electrode, and vacuum dried under 60 ℃. 20 μL of concentrated SHINs solution was then dropped on the black spot formed, and vacuum dried again. After that, the Au electrode was assembled in a spectroelectrochemical cell (Model C031–3, GaossUnion, Hubei, China), and the cell was connected to CHI760 bipotentiostat (Chenhua Instrument Co. Ltd, China). The Raman tests were conducted with a 785 nm laser for excitation, and the ND filter was set to 25%, with an acquisition time of 30 s.

Electrochemical measurements. All electrochemical properties were collected using a three-electrode electrochemical system at room temperature. The electrocatalytic HER was characterized in 1M KOH with a scan rate of 5 mV s^{-1}, and the electropotential for hydrogen evolution was evaluated at 10 and 1000 mA cm^{-2} current density. Furthermore, the HER potentials was converted to standard reversible hydrogen electrode (RHE) scale according to the equation: E (vs. RHE) = E (vs. Hg/HgO) + 0.059*pH + 0.098 V. The polarization curves of the HER was iR-corrected. The Tafel slopes was calculated according to the Tafel equation: $\eta = b\log j + a$, where η is the overpotential, b is the Tafel slope, j is the current density and a is the Tafel intercept relative to the exchange current density j_0. Electrochemical impedance spectroscopy (EIS) measurements were carried out in the frequency range of 10^5 to 0.01 Hz with AC amplitude of 10 mV. The double layer capacitance (C_{dl}) was determined by cyclic voltammetry curves measured by scan rates of 60, 70,80, 90, and 100 mV s^{-1}.

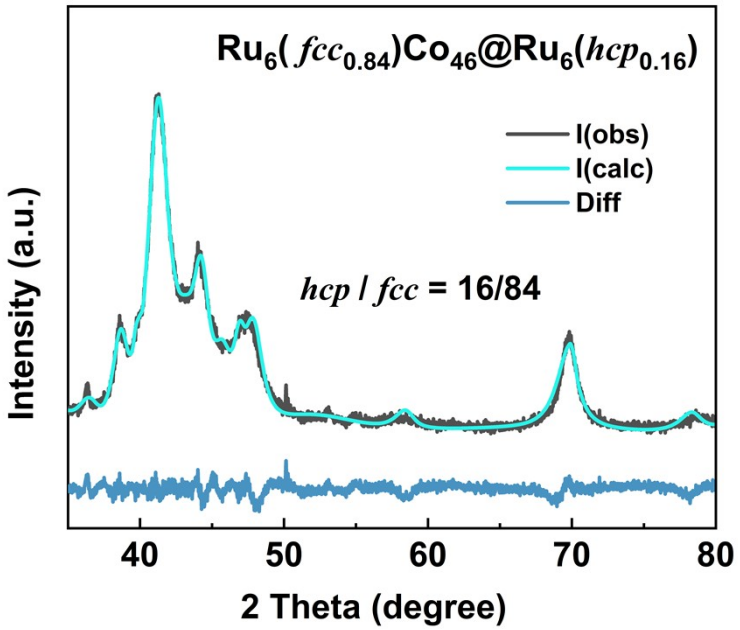

Figure S1. Rietveld refinement of the XRD pattern for the $Ru_6(fcc_{0.84})Co_{46}@Ru_6(hcp_{0.16})$ sample.

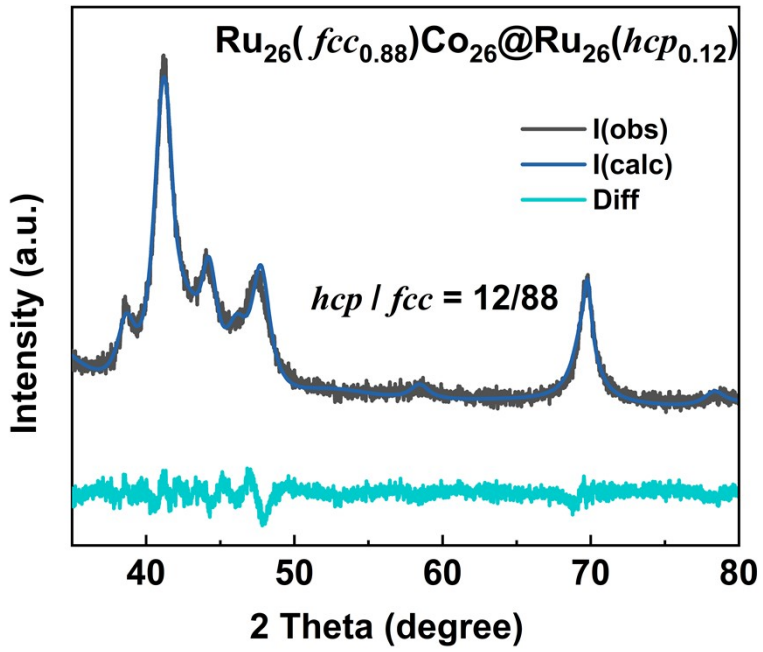

Figure S2. Rietveld refinement of the XRD pattern for the $Ru_{26}($ $fcc_{0.88})Co_{26}@Ru_{26}(hcp_{0.12})$ sample.

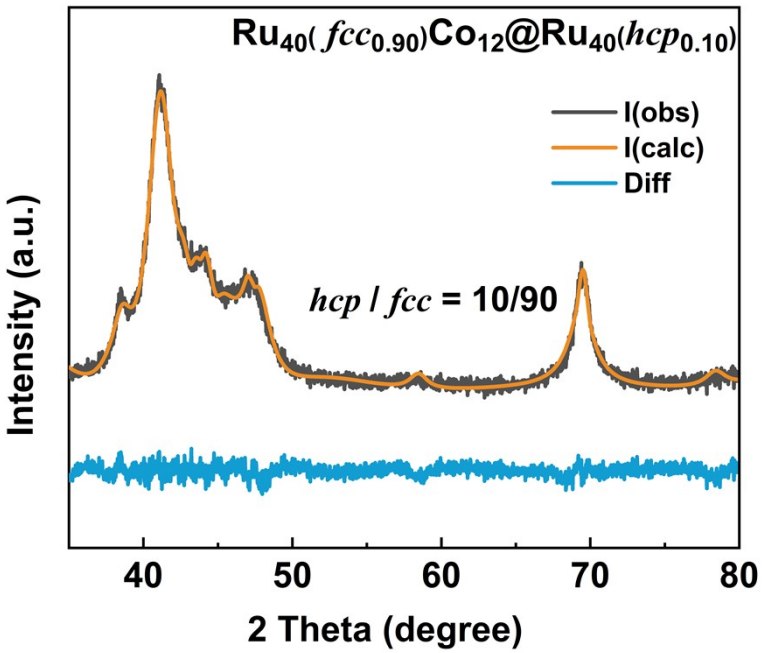

Figure S3. Rietveld refinement of the XRD pattern for the $Ru_{40}($ $fcc_{0.90})Co_{12}@Ru_{40}(hcp_{0.10})$ sample.

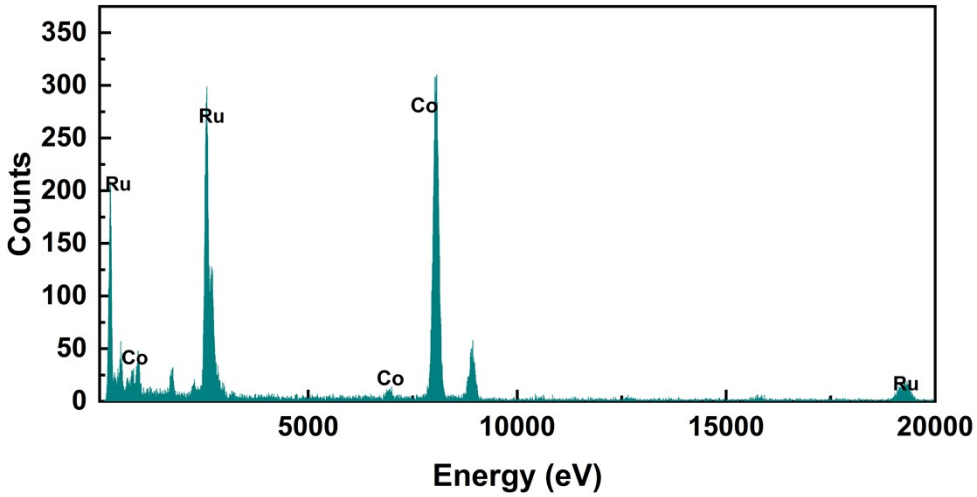

Figure S4. EDX spectrum of $Ru_{12}(fcc_{0.86})Co_{40}@Ru_{12}(hcp_{0.14})$.

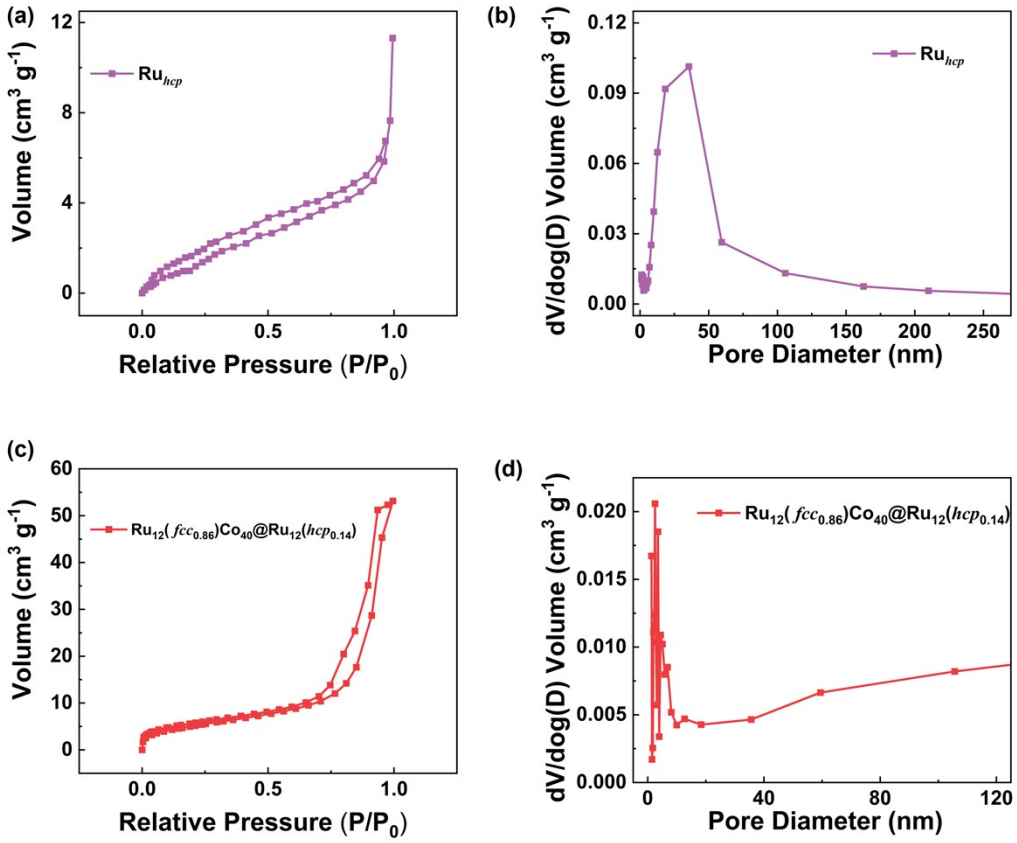

Figure S5. (a,c) N_2 sorption isotherms, (b,d) the pore size distribution derived from adsorption branch of the Ru_{hcp} and $Ru_{12}(fcc_{0.86})Co_{40}@Ru_{12}(hcp_{0.14})$ catalyst.

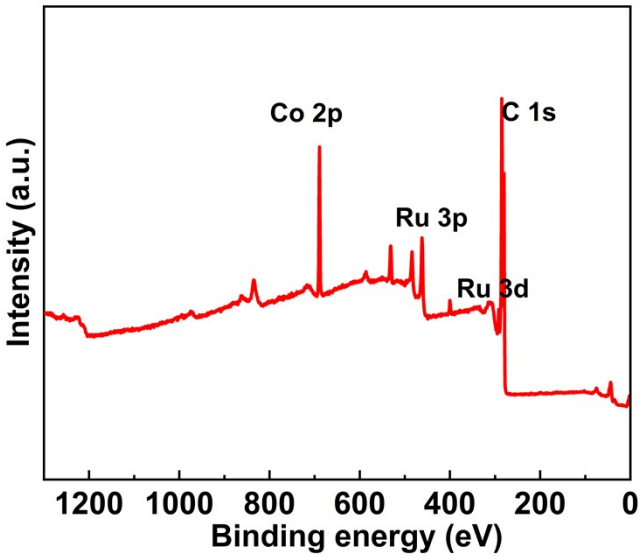

Figure S6. XPS survey spectrum of $Ru_{12}(fcc_{0.86})Co_{40}@Ru_{12}(hcp_{0.14})$.

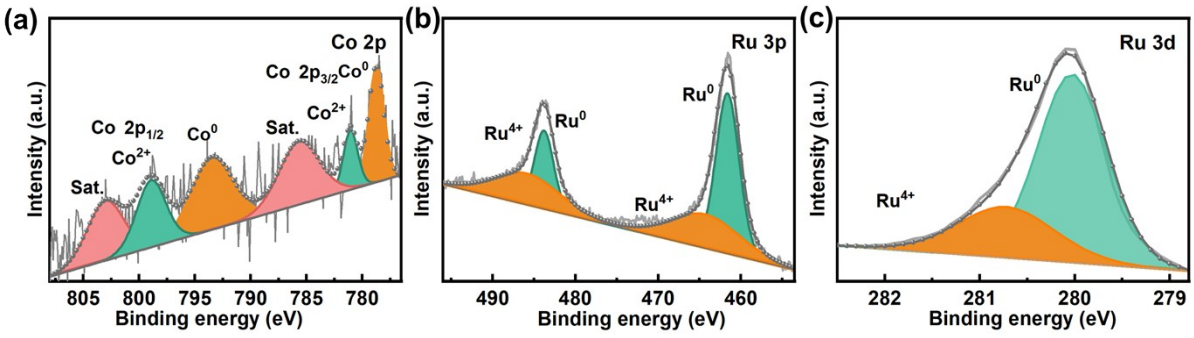

Figure S7. (a) Co 2p, (b) Ru 3p, and (c) Ru 3d XPS spectra of $Ru_{12}(fcc_{0.86})Co_{40}@Ru_{12}(hcp_{0.14})$alloys.

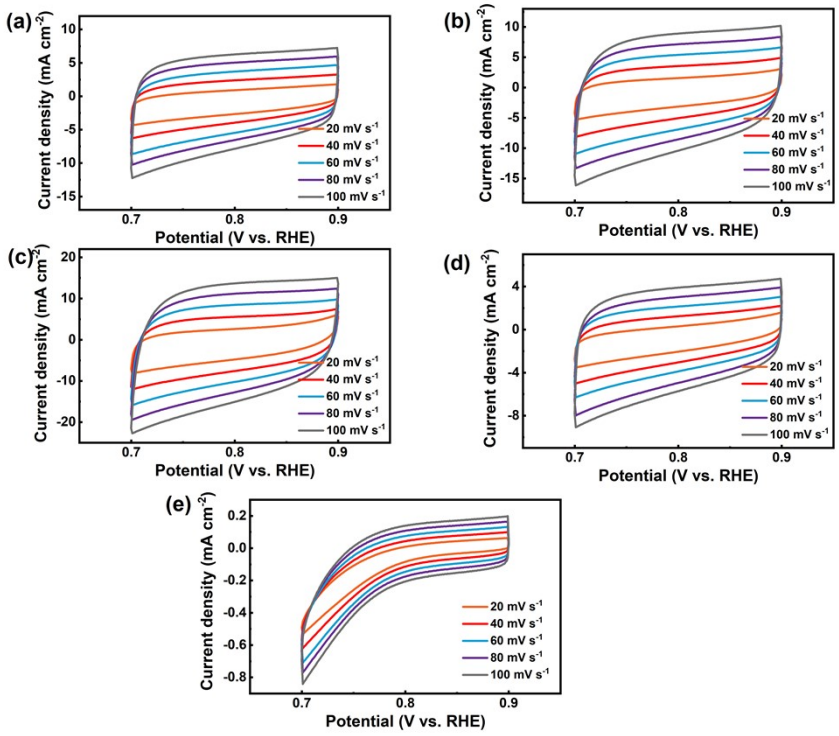

Figure S8. Cyclic voltammograms of (a-e) Ru_6($fcc_{0.84}$)Co_{46}@Ru_6($hcp_{0.16}$),Ru_{12}($fcc_{0.86}$)Co_{40}@Ru_{12}($hcp_{0.14}$), Ru_{26}($fcc_{0.88}$)Co_{26}@Ru_{26}($hcp_{0.12}$), Ru_{40}($fcc_{0.90}$)Co_{12}@Ru_{40}($hcp_{0.10}$), and Ru_{hcp} in the region of 0.7 - 0.9 V versus Hg/HgO at different scan rates.

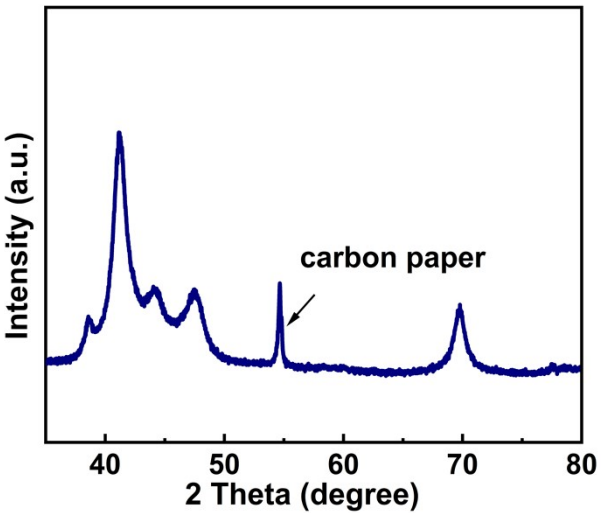

Figure S9. XRD pattern of Ru_{12}($fcc_{0.86}$)Co_{40}@Ru_{12}($hcp_{0.14}$) after HER electrolysis.

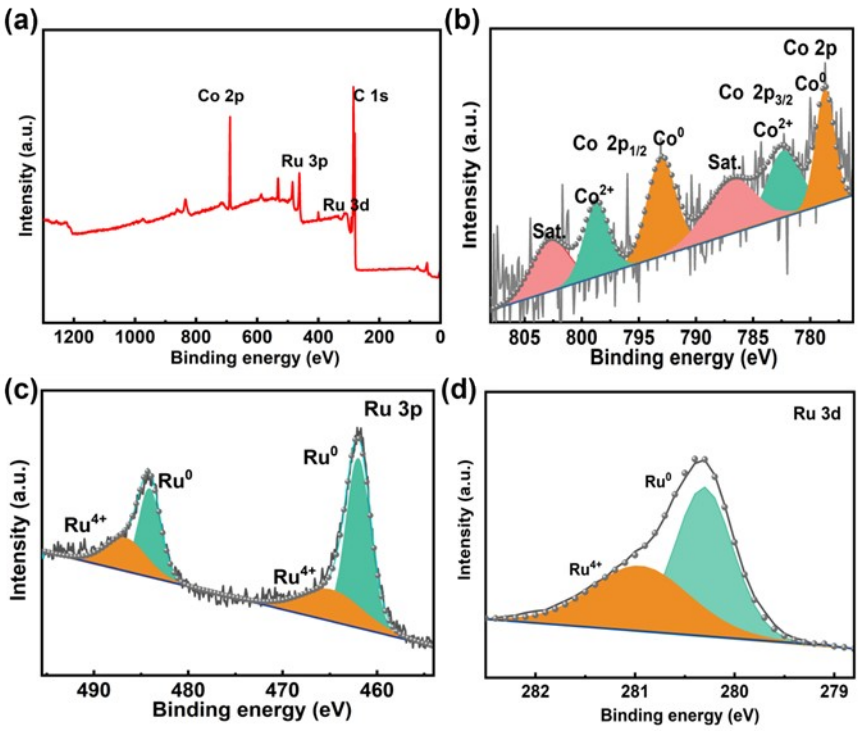

Figure S10. XPS spectrum of $Ru_{12}(fcc_{0.86})Co_{40}@Ru_{12}(hcp_{0.14})$: (a) Survey spectrum and (b) high-resolution Co 2p, Ru 3p, and Ru3d.

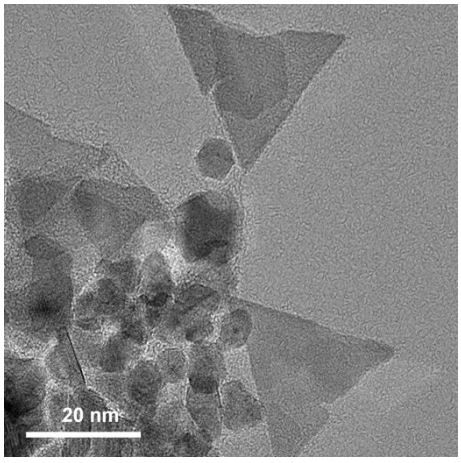

Figure S11. TEM image of $Ru_{12}(fcc_{0.86})Co_{40}@Ru_{12}(hcp_{0.14})$ alloy after HER electrolysis.

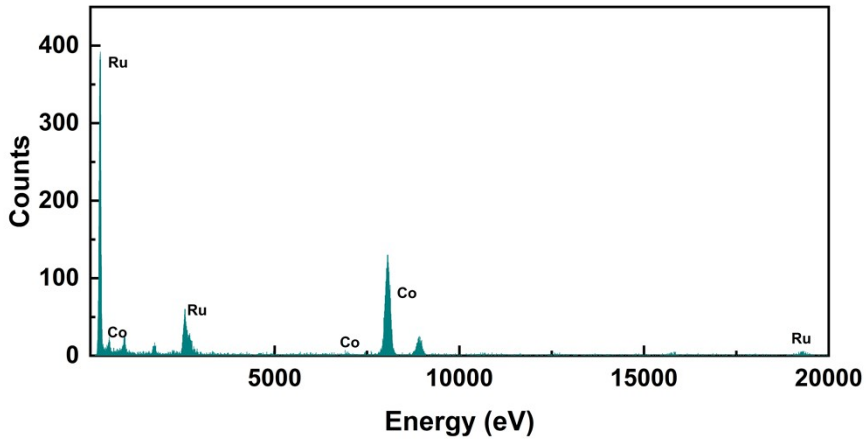

Figure S12. EDX spectrum of $Ru_{12}(fcc_{0.86})Co_{40}@Ru_{12}(hcp_{0.14})$ after HER electrolysis.

Table S1. Co and Ru contents of Ru_{12} ($fcc_{0.86}$)$Co_{40}@Ru_{12}(hcp_{0.14}$) based on the EDX result.

Element	Weight %	Atomic %
Co	2.9	4.9
Ru	97.1	95.1

Table S2. Co and Ru contents of $Ru_6(fcc_{0.84})Co_{46}@Ru_6(hcp_{0.16})$, $Ru_{12}(fcc_{0.86})Co_{40}@Ru_{12}(hcp_{0.14})$, $Ru_{26}(fcc_{0.88})Co_{26}@Ru_{26}(hcp_{0.12})$, and $Ru_{40}(fcc_{0.90})Co_{12}@Ru_{40}(hcp_{0.10})$ based on the ICP result.

	Element	Mass %
$Ru_6(fcc_{0.84})Co_{46}@Ru_6(hcp_{0.16})$	Co	5.6
	Ru	94.4
$Ru_{12}(fcc_{0.86})Co_{40}@Ru_{12}(hcp_{0.14})$	Co	5.0
	Ru	95.0
$Ru_{26}(fcc_{0.88})Co_{26}@Ru_{26}(hcp_{0.12})$	Co	4.9
	Ru	95.1
$Ru_{40}(fcc_{0.90})Co_{12}@Ru_{40}(hcp_{0.10})$	Co	4.8
	Ru	95.2

Table S3. Comparison of HER activity of the reported electrocatalysts in 1.0 M KOH.

Electrocatalysts	E (mV vs. RHE)	Tafel slopes (mv dec^{-1})	References
$Ru_{12}(fcc_{0.86})Co_{40}@Ru_{12}(hcp_{0.14})$	**29.1 mV @ 10 mA cm^{-2}**	**20**	**This work**
Ru-VO_2	46 mV @ 10 mA cm^{-2}	39.1	1
Ru/TiON-C	42 mV @ 10 mA cm^{-2}	40	2
In5	67 mV @ 10 mA cm^{-2}	107	3
$NiCoRu_{0.3}$/SP	59 mV @ 10 mA cm^{-2}	53	4
Ir_2Ni_8/NHCSs	54 mV @ 10 mA cm^{-2}	60	5
MoO_2-FeP@C	103 mV @ 10 mA cm^{-2}	48	6
FeCoNiCuPd	29 mV @ 10 mA cm^{-2}	47.2	7
NiCo DASs/N-C	189 mV @ 10 mA cm^{-2}	72.5	8
Ru/MoO_2	39 mV @ 10 mA cm^{-2}	50	9
PtCoCuNiZn	33 mV @ 10 mA cm^{-2}	35	10

Table S4 Comparison of HER activity of reported electrocatalysts at industrial current densities.

Electrocatalysts	E (mV vs. RHE)	Tafel slopes (mv dec^{-1})	Time	References
$Ru_{12}(fcc_{0.86})Co_{40}@Ru_{12}(hcp_{0.14})$	**377 mV @ 1000 mA cm^{-2}**	**20**	**200 h**	**This work**
MIL-(IrNiFe)@NF	690 mV @ 1000 mA cm^{-2}	53	24 h	11
WMoC	400 mV @ 1000 mA cm^{-2}	65	200 h	12
D-EHEA-$Zr_{0.25}$	370 mV @ 1000 mA cm^{-2}	44.9	150 h	13
Ni_3S_2@LiMoNi$O_x(OH)_y$	365 mV @ 1000 mA cm^{-2}	78.9	100 h	14
Ni_3P/MnOOH	341 mV @ 1000 mA cm^{-2}	81.4	50 h	15
$V_{0.3}Mo_{0.7}B$	452 mV @ 1000 mA cm^{-2}	60	28 h	16
$NiCoS_x$@CoCH NAs/NF	412 mV @ 1000 mA cm^{-2}	63	200 h	17
CoP/MoP@NC/CC	475 mV @ 1000 mA cm^{-2}	52	20 h	18
Sn–Ni_3S_2/NF	570 mV @ 1000 mA cm^{-2}	55.6	60 h	19

IrFe/NC	850 mV @ 1000 mA cm^{-2}	22	12 h	[20]

Table S5. The fitting results of electrochemical element parameters from electrochemical impedance spectroscopy (EIS) for catalysts of HER.

Samples	R_s	R_{ct}	CPE_0
$Ru_{40}(fcc_{0.90})Co_{12}@Ru_{40}(hcp_{0.10})$	4.2	11.9	0.80
$Ru_{26}(fcc_{0.88})Co_{26}@Ru_{26}(hcp_{0.12})$	4.9	7.2	0.67
$Ru_{12}(fcc_{0.86})Co_{40}@Ru_{12}(hcp_{0.14})$	4.5	2.2	0.71
$Ru_{6}(fcc_{0.84})Co_{46}@Ru_{6}(hcp_{0.16})$	4.3	59	0.86
Ru_{hcp}	4.4	110	0.73

R_s shows the resistance of the electrolyte and intrinsic resistance of the active materials on the electrode. R_{ct} represents charge transfer resistance, which determines the interfacial electron.

References

1. Z. Niu, Z. Lu, Z. Qiao, S. Wang, X. Cao, X. Chen, J. Yun, L. Zheng and D. Cao, Adv. Mater., 2023, 36, 2310690.
2. M. Smiljanić, M. Bele, L. Pavko, A. Hrnjić, F. Ruiz-Zepeda, L. Bijelić, A. R. Kamšek, M. Nuhanović, A. Marsel, L. Gašparič, A. Kokalj and N. Hodnik, Chem. Engin. J., 2025, 517, 164204.
3. S. Mondal, S. Dutta, S. Mal, S. K. Pati and S. Bhattacharyya, Angew. Chem. Int. Ed. Engl., 2023, 62, e202301269.
4. L. Li, H. Qiu, Y. Zhu, G. Chen, S. She, X. Guo, H. Li, T. Liu, Z. Lin, H. Zhou, Y. Zhu, M. Yang, B. Xu and H. Huang, Appl Catal, B-Environ, 2023, 331, 117965.
5. N. Wei, M. Mao, J. Wu, Y. Long and G. Fan, Fuel, 2022, 319, 123637.
6. G. Yang, Y. Jiao, H. Yan, Y. Xie, A. Wu, X. Dong, D. Guo, C. Tian and H. Fu, Adv. Mater., 2020, 32, 2000455.
7. S. Wang, B. Xu, W. Huo, H. Feng, X. Zhou, F. Fang, Z. Xie, J. K. Shang and J. Jiang, Appl Catal, B-Environ, 2022, 313, 121472.
8. M. Li, H. Zhu, Q. Yuan, T. Li, M. Wang, P. Zhang, Y. Zhao, D. Qin, W. Guo, B. Liu, X. Yang, Y. Liu and Y. Pan, Adv. Funct. Mater., 2022, 33, 2210867.
9. P. Ren, W. Wang, Y. Hong, Y. Zheng, X. Ren, W. Du, Y. Chen, S. Tan and W. Zhang, ACS Appl. Nano Mater., 2023, 6, 13926-13934.
10. H. Ren, Z. Zhang, Z. Geng, Z. Wang F. Shen, X. Liang, Z. Cai, Y. Wang, D. Cheng, Y. Cao, X. Yang, M. Hu, X. Yao and K. Zhou, Adv. Energy Mater., 2024, 14, 240077.
11. Q. Kong, C. Yu, Q. Lu, X. Yang, T. Xu, Q. Song, H. Li, Z. H. Liu, Q. Qiao, G. He, Y. Wang, L. Yao, X. Dai and X. Zhang, Small, 2025, 21, 2503398.
12. L. Shen, Y. Shi, T. O. Ogundipe, K. Huang, S. Cao, Z. Lu, Z. Wang, H. Tan and C. Yan, J. Power

Sources, 2022, 538, 231557.
13. Q. Zhang, Q. Guo, Y. Zhang, Y. He, W. Gong, W. Liu, X. Liu and R. Li, Adv. Funct. Mater., 2024, 35, 2414446.
14. Q.-N. Ha, N. Susanto Gultom, M. Zefanya Silitonga, T. Negash Gemeda and D.-H. Kuo, Chem. Eng. J., 2023, 467, 143253.
15. P. Jiang, H. Huang, J. Diao, S. Gong, S. Chen, J. Lu, C. Wang, Z. Sun, G. Xia, K. Yang, Y. Yang, L. Wei and Q. Chen, Appl. Catal, B-Environ., 2019, 258, 117965.
16. C. Zhang, Y. Luo, J. Tan, Q. Yu, F. Yang, Z. Zhang, L. Yang, H.-M. Cheng and B. Liu, Nat. Commun., 2020, 11, 3724.
17. C. Li, Z. Wang, M. Liu, E. Wang, B. Wang, L. Xu,K. Jiang, S. Fan, Y. Sun, J. Li and K. Liu, Nat. Commun., 2022, 13, 3338.
18. Y. Cheng, H. Chen, L. Zhang, X. Xu, H. Cheng, C. Yan and T. Qian, Adv. Mater., 2024, 36, 2313156.
19. Z. Zheng, L. Yu, M. Gao, X. Chen, W. Zhou, C. Ma, L. Wu, J. Zhu, X. Meng, J. Hu, Y. Tu, S. Wu, J. Mao, Z. Tian and D. Deng, Nat. Commun., 2020, 11, 3315.
20. R. Liu, Z. Gong, J. Liu, J. Dong, J. Liao, H. Liu, H. Huang, J. Liu, M. Yan, K. Huang, H. Gong, J. Zhu, C. Cui, G. Ye and H. Fei, Adv. Mater., 2021, 33, 2103533.